

Rapid fabrication of $\text{Fe}_x\text{Ni}_{2-x}\text{P}_4\text{O}_{12}$ and graphene hybrids as electrocatalyst for highly efficient oxygen evolution reaction

Lu Lin ^a, Yufeng Wang ^a, Qing Ye ^a, Yanxia Zhao ^{a,*}, Yongliang Cheng ^{a,b,**}

^a Key Laboratory of Synthetic and Natural Functional Molecule of the Ministry of Education, College of Chemistry and Materials Science, Northwest University, Xi'an 710127, China

^b Shaanxi Key Laboratory for Carbon Neutral Technology, Northwest University, Xi'an 710127, China



ARTICLE INFO

Keywords:

Microwave
Transition metal phosphate
Graphene
Electrocatalyst
Oxygen evolution reaction

ABSTRACT

Transition metal phosphates have been considered as a kind of promising electrocatalysts towards oxygen evolution reaction (OER), however, the unsatisfactory OER activity and tedious preparation process greatly restrict their further application. Herein, we report a novel microwave assistant strategy to fabricate graphene supported $\text{Fe}_x\text{Ni}_{2-x}\text{P}_4\text{O}_{12}$ ($\text{Fe}_x\text{Ni}_{2-x}\text{P}_4\text{O}_{12}/\text{RGO}$) hybrids as OER electrocatalyst. In alkaline solution, the optimized $\text{Fe}_x\text{Ni}_{2-x}\text{P}_4\text{O}_{12}/\text{RGO}$ merely needs low overpotential of 277, 340 and 380 mV to achieve 100, 500 and 1000 mA cm^{-2} , respectively. Moreover, the electrolytic cell assembled by $\text{Fe}_x\text{Ni}_{2-x}\text{P}_4\text{O}_{12}/\text{RGO}$ and Pt/C only requires voltage of 1.549, 1.678 and 1.773 V to generate 100, 500 and 1000 mA cm^{-2} , respectively, outperforming the electrolytic cell assembled by IrO_2 and Pt/C. Durability test at 100 mA cm^{-2} for 100 h displays no obvious degradation of activity, confirming its outstanding stability. The strategy presented in this work affords a new avenue to fabricate high performance electrocatalysts.

1. Introduction

Hydrogen, as a type of green energy carrier with high energy density, clean combustion and sustainability, receives tremendous attentions and is considered as one of the best alternative to fossil fuels [1–3]. Electrocatalytic water splitting driven by renewable energy is an effective approach to produce hydrogen [4]. However, the oxygen evolution reaction (OER) with the sluggish four-electron transfer process usually leads to high overpotential and low energy utilization efficiency, consequently, greatly inhibiting the practical application of water splitting [5]. At present, the best active Ru/Ir based electrocatalyst faces the bottleneck of large-scale application due to their scarce reserves and high cost [6]. Therefore, it is urgent to design highly active non-precious based OER electrocatalyst to realize the large-scale application of water splitting.

Recently, transition metal phosphates, due to their specific physical and chemical properties, have gained considerable attention as advanced OER electrocatalyst. The phosphate group with flexible coordination feature can effectually stabilize the intermediate state of active center, conduced to effective redox reaction of active center [7].

Besides, the phosphate group can also serve as proton acceptors to accelerate the proton-coupled electron transfer kinetics as well as induce distorted local metal geometry, which can contribute to favorable water adsorption and subsequent oxidation [8,9]. Therefore, various phosphates based OER electrocatalysts, such as $\text{Ni}_2\text{P}_4\text{O}_{12}$ [9,10], $\text{Mn}_3(\text{PO}_4)_2$ [11], $\text{Fe}_3\text{Co}(\text{PO}_4)_4$ [12] and $\text{Co}_2\text{P}_2\text{O}_7$ [13] have been reported and demonstrated superior OER activity. In particular, cyclotetraphosphates have received more and more attention because their abundant polar phosphate groups and higher P content are beneficial to enhance OER activity [14–17]. Despite the remarkable inspiring progress, the application of phosphates still faces several issues to be addressed. First, their OER activity is still unsatisfactory for practical application. Generally, the OER activity of electrocatalysts is principally determined by their adsorption capability for oxygen-containing intermediates. The affinity of phosphate for OH groups can facilitate the adsorption of water, but can also cause to strong adsorption for oxygen-containing intermediates [18], thus resulting in inferior OER activity. Second, hydrothermal and high-temperature treatment is mainly strategy for fabricating phosphates [8,9,19,20]. Most of them need long time operation, causing to excessive consumption of time and energy. Additionally, the

* Corresponding author.

** Corresponding author at: Key Laboratory of Synthetic and Natural Functional Molecule of the Ministry of Education, College of Chemistry and Materials Science, Northwest University, Xi'an 710127, China.

E-mail addresses: zhaoyxcas2008@163.com (Y. Zhao), ycheng@nwu.edu.cn (Y. Cheng).

high-temperature treatment may bring about severe aggregation of nanoparticle, reducing the expose of active sites. Third, the conductivity of phosphates is relatively poor, which greatly restricts their OER activity. Last but not least, hypophosphite is the most popular phosphorus sources for fabricating phosphates [9,17,20–22]. The decomposition of hypophosphite usually generates toxic PH₃ gas, which is also a great disadvantage for their large-scale application.

Inspired by aforementioned considerations, herein, we develop a novel and facile microwave assistant strategy to fabricate reduced graphene oxide supported Fe_xNi_{2-x}P₄O₁₂ (Fe_xNi_{2-x}P₄O₁₂/RGO) hybrids as OER electrocatalyst. Especially, the overall heating treatment process was achieved within 75 s, which can avoid long heating period and high energy consumption caused by conventional heating method. Besides, as a green phosphorus source that can be obtained from grains and plant seeds, phytic acid (PA) was chosen as phosphorus source, which can avoid the release of toxic PH₃ gas resulted from the decomposition of hypophosphite, which are beneficial to their practical application. Furthermore, benefitting from the enhanced electronic conductivity contributed by coupling with RGO and optimized electronic structure caused by introducing of Fe, the optimized Fe_xNi_{2-x}P₄O₁₂/RGO demonstrates good OER activity, requiring a overpotential of 273 mV at 10 mA cm⁻², outperforming the sample synthesized by conventional high-temperature treatment method. Remarkably, the activity of Fe_xNi_{2-x}P₄O₁₂/RGO can be further improved when it was loaded on Ni fibers felt (NFF), only small overpotential of 277, 340 and 380 mV were required to generate 100, 500 and 1000 mA cm⁻², respectively, which is prominently superior to IrO₂. Moreover, the electrolytic cell assembled by Fe_xNi_{2-x}P₄O₁₂/RGO and Pt/C can achieve 100, 500 and 1000 mA cm⁻² at cell voltage of 1.549, 1.678 and 1.773 V, respectively. Additionally, the assembled electrolytic cell can steadily operate for 100 h at 100 mA cm⁻² without apparent degradation of activity. Our work provides a highly active OER electrocatalyst, as well as a novel avenue to fabricate phosphate based electrocatalyst.

2. Experimental section

2.1. Preparation of Fe_xNi_{2-x}P₄O₁₂/RGO

For preparing Fe_xNi_{2-x}P₄O₁₂/RGO, 100 mg of graphene oxide (GO) was firstly dispersed in 30 mL of ethanol by ultrasonic dispersion for 1 h under ice-water bath. Then, 0.471 g of Ni(NO₃)₂·6H₂O and 0.117 g of Fe (NO₃)₃·9H₂O were added in above dispersion. Thereafter, 3.3 mL of PA was added. After stirring for 2 h under room temperature, Ni²⁺/Fe³⁺-PA/GO hybrids were collected by centrifuging, washing with ethanol and deionized water by several times and drying under vacuum for 12 h. Finally, the obtained powder was transferred into a quartz beaker for microwave irradiation treatment in air atmosphere to generate Fe_xNi_{2-x}P₄O₁₂/RGO. Here, a copper mesh was employed as a blasting fuse for microwave treatment.

2.2. Preparation of Fe_xNi_{2-x}P₄O₁₂

0.471 g of Ni(NO₃)₂·6H₂O and 0.117 g of Fe (NO₃)₃·9 H₂O were firstly dissolved in the solvent consisting by 30 mL of ethanol and 1 mL of deionized water. Then, 3.3 mL of PA was added. After 2 h stirring, the Ni²⁺/Fe³⁺-PA coordination compound were collected by centrifuging, washing with ethanol and deionized water by several times and drying under vacuum for 12 h. Finally, the obtained powder was subjected to microwave irradiation treatment under the same conditions used for synthesizing Fe_xNi_{2-x}P₄O₁₂/RGO.

2.3. Material characterization

The crystalline structure and phase composition of the samples were analyzed by X-ray diffraction (XRD, Bruker D8 Advance diffractometer). The morphology and microstructure of the samples were characterized

by scanning electron microscopy (SEM, Hitachi S-8100) and transmission electron microscopy (TEM Talos F200X) coupled with energy dispersive spectroscopy (EDS). The surface chemical composition and valence states of the electrocatalysts were investigated by X-ray photo-electron spectroscopy (XPS, ThermoFisher ESCALAB 250Xi). The total carbon content in the electrocatalyst was analyzed by thermogravimetry analysis (TGA, Netzsch STA 449 C). The atomic ratios of the electrocatalyst and element content of the electrolyte before and after long-term OER test was analyzed by inductively coupled plasma mass spectrometry (ICP-MS, Agilent 7900). The specific surface area and pore size distribution of the electrocatalyst were determined by N₂ adsorption-desorption tests using a porosity analyzer (ASAP 2460, Micromeritics).

2.4. Electrochemical measurements

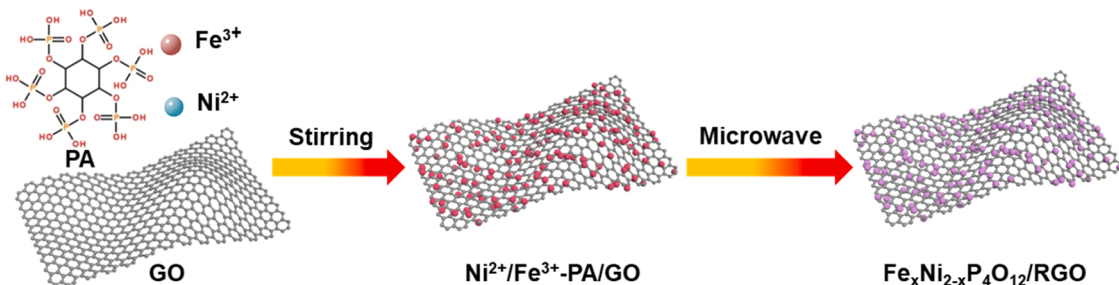
A typical three-electrode system in 1 M KOH electrolyte was employed to evaluate the OER performance of the sample, where, Hg/HgO electrode, graphite rod and glass carbon electrode (diameter, 3 mm) was utilized as reference electrode, counter electrode and working electrode, respectively. All potentials were calibrated to reverse hydrogen electrode (RHE) according to the equation: E_{RHE} = E_{Hg/HgO} + 0.924 and corrected through iR compensation. The working electrode was prepared by dropping 5 μ L of the electrocatalyst dispersion onto the glassy carbon electrode surface. The dispersion was comprised of 2.5 mg of the sample, 0.375 mg of carbon black, 10 μ L of nafion solution (5 wt %,) and 490 μ L of isopropanol. The liner sweep voltammetry (LSV) curves were collected with a scan rate of 5 mV s⁻¹. Cyclic voltammetry (CV) measurements with different scanning rate were carried out to obtain electrochemical double-layer capacitance (C_{dL}) of the electrocatalysts. Electrochemical impedance spectroscopy (EIS) tests were carried out with 5 mV amplitude in the frequency range from 0.1 to 10⁵ Hz. Chronopotentiometric test at a constant current density and continuous CV scanning were employed to evaluate the durability of the electrocatalyst.

3. Results and discussion

3.1. Material fabrication and characterizations

The typical procedure for preparing Fe_xNi_{2-x}P₄O₁₂/RGO hybrids is displayed in Scheme 1. Firstly, metal salts were added in the homogeneous GO dispersion, the metal ions (Ni²⁺ and Fe³⁺) can be adsorbed on GO surface via electrostatic interaction due to their abundant oxygen-containing functional group on GO surface. Then, PA was poured into above dispersion, the metal ions would further complex with PA to form Ni²⁺/Fe³⁺-PA coordination compound [23,24]. At last, the obtained Ni²⁺/Fe³⁺-PA/GO hybrids were subjected to microwave irradiation treatment. During above process, the high temperature can be immediately achieved [25], resulting in the reduction of GO and the decomposition of Ni²⁺/Fe³⁺-PA coordination compound to generate Fe_xNi_{2-x}P₄O₁₂/RGO hybrids. Meanwhile, the pyrolysis of PA also can produce carbon containing P, which is also beneficial to inhibit the agglomeration of catalyst nanoparticle.

The morphological and microstructural information of the prepared electrocatalysts were detected by SEM and TEM. The Ni²⁺/Fe³⁺-PA/GO hybrids exhibit sheet-like morphology with smooth surface (Fig. S1 and S2a). The high-resolution TEM (HRTEM) image (Fig. S2b) displays no obvious lattice fringes, indicating the amorphous structure of Ni²⁺/Fe³⁺-PA coordination compound. Additionally, high-angle annular dark field scanning TEM (HAADF-STEM) and corresponding EDS mapping images (Fig. S2c) reveal the existence of Ni, Fe and P element on GO surface, which demonstrates the formation of Ni²⁺/Fe³⁺-PA coordination compound on the surface of GO. In addition, many sheets constituted by agglomerated nanoparticles can be obtained after pyrolysis of Ni²⁺/Fe³⁺-PA/GO hybrids through conventional heating method in air



Scheme 1. A schematic illustration of the synthesis process for $\text{Fe}_x\text{Ni}_{2-x}\text{P}_4\text{O}_{12}/\text{RGO}$.

atmosphere (Fig. S3), which further confirms the formation of $\text{Ni}^{2+}/\text{Fe}^{3+}$ -PA coordination compound on GO surface. After microwave irradiation of $\text{Ni}^{2+}/\text{Fe}^{3+}$ -PA/GO hybrids, many $\text{Fe}_x\text{Ni}_{2-x}\text{P}_4\text{O}_{12}$ nanoparticles are uniformly formed on RGO surface (Figs. 1a-1c). TEM image with high-magnification reveals that the $\text{Fe}_x\text{Ni}_{2-x}\text{P}_4\text{O}_{12}$ nanoparticles display noteworthy difference on contrast (Fig. 1d). The clear lattice stripes with spacing of 0.298 nm are observed in dark-colored region of the nanoparticle, which is attributed to the (-113) planes of $\text{Ni}_2\text{P}_4\text{O}_{12}$, however, no lattice fringes were found in light-colored region of

nano particle, indicating its amorphous structure. The formation of amorphous/crystalline interface are conducive to expose active sites [26]. The elemental mapping of $\text{Fe}_x\text{Ni}_{2-x}\text{P}_4\text{O}_{12}/\text{RGO}$ was further collected to analyze the elemental distribution. HAADF-STEM and corresponding EDS mapping images confirm the existence of Ni, Fe, P and O and the intensity of Ni in crystalline region is obviously higher than that in amorphous region. This phenomenon was further demonstrated by corresponding elemental linear scanning analysis (Fig. S4). This uneven distribution of element may also make for regulating electronic structure

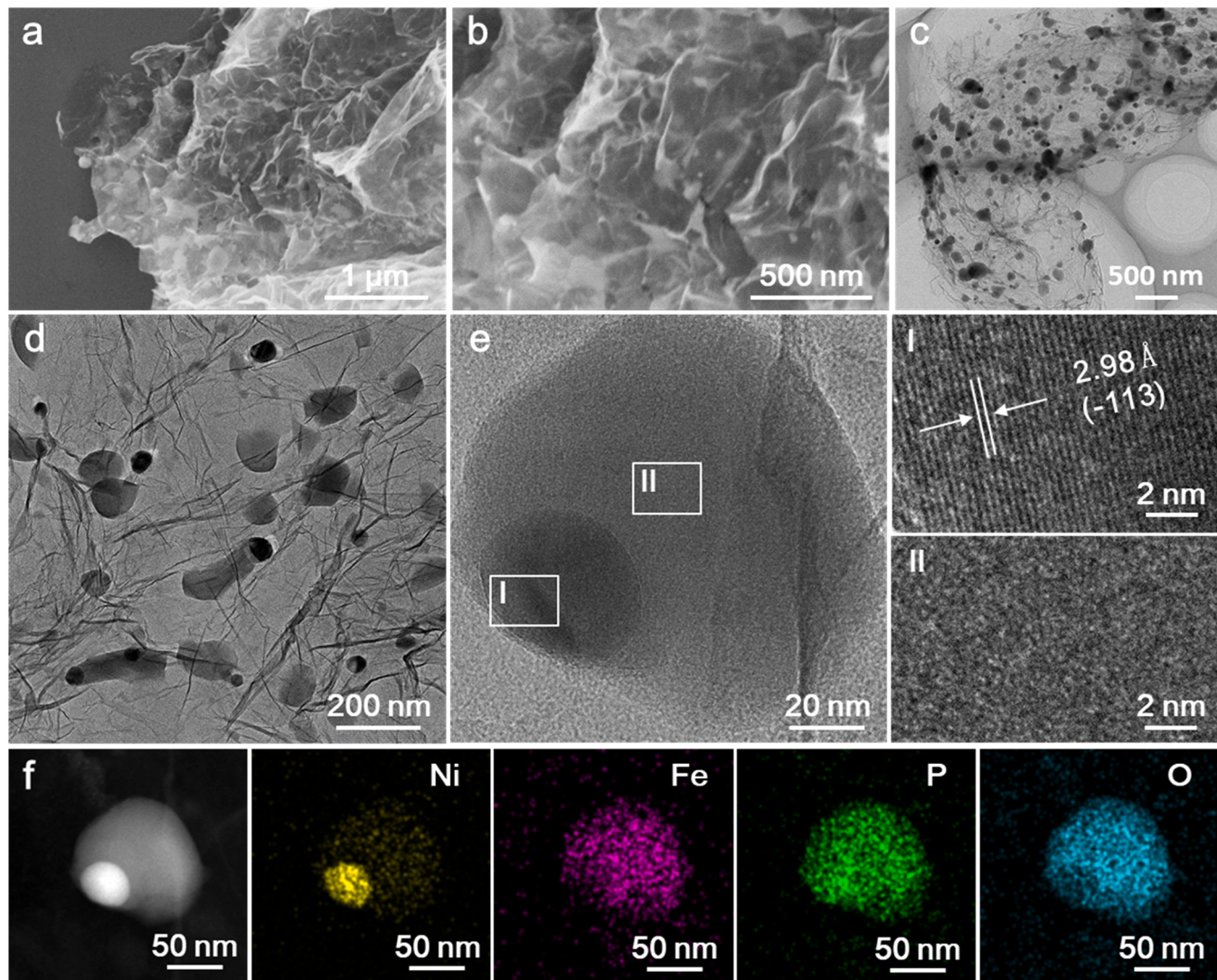


Fig. 1. (a) low- and (b) high-magnification SEM image of $\text{Fe}_x\text{Ni}_{2-x}\text{P}_4\text{O}_{12}/\text{RGO}$, (c) low- and (b) high-magnification TEM images of $\text{Fe}_x\text{Ni}_{2-x}\text{P}_4\text{O}_{12}/\text{RGO}$, (e) HRTEM and (f) HAADF-STEM and corresponding EDS mapping images of $\text{Fe}_x\text{Ni}_{2-x}\text{P}_4\text{O}_{12}/\text{RGO}$.

and facilitating electron transportation, favoring for improving OER activity [27]. The ratio of Ni:Fe in crystalline and amorphous region are 7.1:1 and 0.48:1 based on the mapping analysis (Fig. S5 and Table S1), respectively. The ratio of Ni:Fe in whole nanoparticles is 1.09:1, which is consistent with the results of ICP-MS (1.16:1). Interestingly, this uneven distribution of element was not observed in the sample fabricated by just adding Fe^{3+} salt (Fig. S6 and S7). In addition, some dark-colored region containing P element can be found on RGO (denoted as P-RGO) surface when only adding PA during synthesis process (Fig. S8), which is significantly difference from the RGO fabricated by microwave irradiation of pure GO (Fig. S9). These results suggest that PA molecule can also be adsorbed on GO surface, which would further competitive adsorb metal ions with the oxygen-containing functional group on GO surface. To further explore the formation mechanism of this uneven distribution of element, $\text{Ni}^{2+}/\text{Fe}^{3+}$ -PA/GO hybrids were also carbonized in Ar atmosphere through conventional heating method. The corresponding TEM characterizations clearly demonstrate the uniformly distributed Ni and Fe element (Fig. S10). Therefore, the unevenly distributed Ni and Fe element can be attributed to their different coordination interaction force with PA and oxygen-containing functional group on GO surface, which lead to different migration rate of metal ions during microwave irradiation treatment, thus resulting in the uneven distribution of element [28,29]. For conventional heating treatment, long-time heating can ensure metal ions have sufficient time to migrate and form uniformly distributed element. The aforementioned results elucidate that different heating treatment approach has a prominent effects on the interior structure of the electrocatalysts, thus leading to different OER activities [30].

The crystalline structure and chemical state of the as-fabricated samples were investigated by XRD and XPS. As presented in Fig. S11,

no diffraction peaks can be observed in the XRD patterns of the samples synthesized by microwave irradiation of Fe^{3+} -PA/GO hybrids, indicating their amorphous structure, which is agreed well with the TEM characterization. This sample was denoted as $\text{FeP}_x\text{O}_y/\text{RGO}$ due to the presence of P-O bonding, as demonstrated by the following XPS discussions. For microwave irradiated Ni^{2+} -PA/GO and $\text{Ni}^{2+}/\text{Fe}^{3+}$ -PA/GO samples, the mainly diffraction peaks can be identified to $\text{Ni}_2\text{P}_4\text{O}_{12}$ (Fig. 2a and S12a). The intensity of diffraction peaks of $\text{Fe}_x\text{Ni}_{2-x}\text{P}_4\text{O}_{12}/\text{RGO}$ distinctly decrease in comparison with $\text{Ni}_2\text{P}_4\text{O}_{12}$ and $\text{Fe}_x\text{Ni}_{2-x}\text{P}_4\text{O}_{12}$ (Fig. S12b), indicating their relatively poor crystallinity. This can be attributed to the change of growth and evolution of nanocrystal caused by graphene support [31]. The broad diffraction peak around at $\sim 26^\circ$ is assigned to (002) face of the graphitized carbon [32]. The total carbon content including RGO and that derived from PA in $\text{Fe}_x\text{Ni}_{2-x}\text{P}_4\text{O}_{12}/\text{RGO}$ was calculated to be 44% based on TG analysis and XRD characterization (Fig. S13). In the Ni 2p spectra of $\text{Fe}_x\text{Ni}_{2-x}\text{P}_4\text{O}_{12}/\text{RGO}$ (Fig. 2b), the fitted peaks located at 856.90 and 874.78 eV are characteristic peaks of Ni^{2+} and the other two peaks at 861.77 and 879.87 eV are indexed to their satellite peaks [33]. The binding energy of Ni^{2+} in Ni 2p_{3/2} region of $\text{Fe}_x\text{Ni}_{2-x}\text{P}_4\text{O}_{12}/\text{RGO}$ is higher than that in $\text{Ni}_2\text{P}_4\text{O}_{12}/\text{RGO}$ (856.82 eV), indicating that the some electron transfers from Ni to Fe. For Fe 2p spectra of $\text{Fe}_x\text{Ni}_{2-x}\text{P}_4\text{O}_{12}/\text{RGO}$ (Fig. 2c), the two dominating fitted peak located at 713.08 and 726.33 eV are assigned to Fe^{3+} and the extra two peaks at 716.69 and 728.60 eV belong to their corresponding satellite peaks [34]. Compared with the $\text{FeP}_x\text{O}_y/\text{RGO}$, the binding energy of Fe^{3+} in Fe 2p_{3/2} region shifts toward lower binding energy position. Additionally, the P 2p spectra of $\text{Fe}_x\text{Ni}_{2-x}\text{P}_4\text{O}_{12}/\text{RGO}$ exhibit only one fitted peak at 134.24 eV, which can be designated to P-O bonding [10,35]. Interestingly, the P 2p spectra of $\text{Fe}_x\text{Ni}_{2-x}\text{P}_4\text{O}_{12}/\text{RGO}$ also present a positive and negative shift relative to

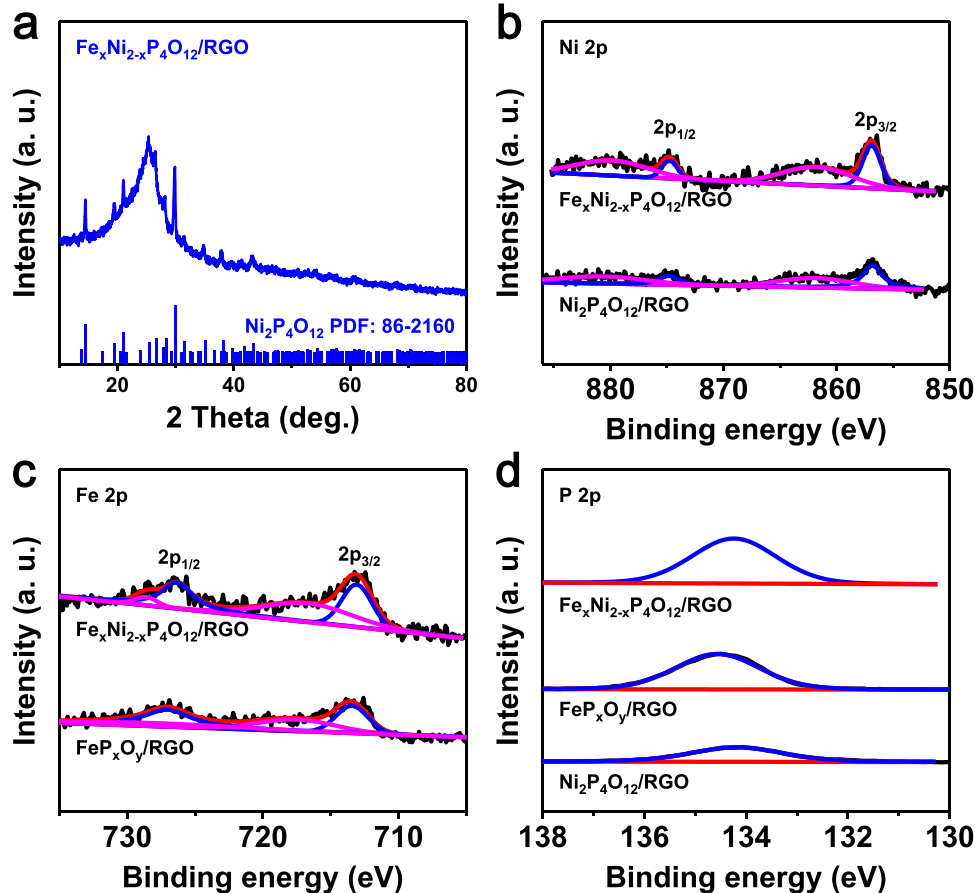


Fig. 2. (a) XRD patterns of $\text{Fe}_x\text{Ni}_{2-x}\text{P}_4\text{O}_{12}/\text{RGO}$, (b) Ni 2p spectra of $\text{Ni}_2\text{P}_4\text{O}_{12}/\text{RGO}$ and $\text{Fe}_x\text{Ni}_{2-x}\text{P}_4\text{O}_{12}/\text{RGO}$, (c) Fe 2p spectra of $\text{FeP}_x\text{O}_y/\text{RGO}$ and $\text{Fe}_x\text{Ni}_{2-x}\text{P}_4\text{O}_{12}/\text{RGO}$ and (d) P 2p spectra of $\text{Ni}_2\text{P}_4\text{O}_{12}/\text{RGO}$, $\text{FeP}_x\text{O}_y/\text{RGO}$ and $\text{Fe}_x\text{Ni}_{2-x}\text{P}_4\text{O}_{12}/\text{RGO}$.

$\text{Ni}_2\text{P}_4\text{O}_{12}/\text{RGO}$ and $\text{FeP}_x\text{O}_y/\text{RGO}$, respectively, further confirming the modulated electronic structure caused by introducing of Fe.

3.2. Electrocatalytic OER performance

The OER activities of the as-synthesized samples were assessed by a three-electrode system. The OER activities of the $\text{Fe}_x\text{Ni}_{2-x}\text{P}_4\text{O}_{12}/\text{RGO}$ synthesized by different microwave irradiation time (60, 75 and 90 s) were firstly investigated to optimize microwave irradiation time. As revealed by the LSV curves in Fig. S14, $\text{Fe}_x\text{Ni}_{2-x}\text{P}_4\text{O}_{12}/\text{RGO}$ with a microwave irradiation time of 75 s exhibits the best OER activity in comparison with that synthesized by microwave irradiation time of 60 s and 90 s, suggesting that the microwave treatment time has an important effect on improvement of the OER activity. Prolonging microwave irradiation time can cause to form larger nanoparticle (Fig. S15), which is unfavorable for charge transfer and active sites exposure (Fig. S16), thus, leading to inferior OER activity. Then the activity of $\text{Fe}_x\text{Ni}_{2-x}\text{P}_4\text{O}_{12}/\text{RGO}$ and the controlled samples were further evaluated. Unless otherwise stated, all the samples were synthesized by microwave irradiation of 75 s. As shown in Fig. 3a, $\text{Fe}_x\text{Ni}_{2-x}\text{P}_4\text{O}_{12}/\text{RGO}$ exhibits a low overpotential of 270 mV at 10 mA cm^{-2} , which significantly

outperforms the controlled samples (313 mV for $\text{Ni}_2\text{P}_4\text{O}_{12}/\text{RGO}$, 519 mV for $\text{FeP}_x\text{O}_y/\text{RGO}$) and IrO_2 (317 mV). As a further comparison, P-RGO exhibits a very poor OER activity (Fig. S17), indicating that the $\text{Fe}_x\text{Ni}_{2-x}\text{P}_4\text{O}_{12}$ is the prominent active species towards OER and the prominently improved OER activity of $\text{Fe}_x\text{Ni}_{2-x}\text{P}_4\text{O}_{12}/\text{RGO}$ mainly originates from the interaction between Ni and Fe. Note that, the $\text{Fe}_x\text{Ni}_{2-x}\text{P}_4\text{O}_{12}/\text{RGO}$ also presents higher OER activity than that without addition of PA during synthesis process (Fig. S18), demonstrating the positive role of phosphorus groups on the enhancement of OER activity. The OER activity of $\text{Fe}_x\text{Ni}_{2-x}\text{P}_4\text{O}_{12}/\text{RGO}$ increases and then decreases with increasing Fe^{3+} addition ratio and the sample with the $\text{Ni}^{2+}/\text{Fe}^{3+}$ addition ratio of 85:15 displays the best OER activity (Fig. S19). More importantly, this activity is also superior to that of the samples fabricated by conventional high-temperature treatment method (Fig. S20). The above results successfully confirm the advantage of microwave irradiation in the synthesis of electrocatalyst.

To rationalize the enhanced OER activity of $\text{Fe}_x\text{Ni}_{2-x}\text{P}_4\text{O}_{12}/\text{RGO}$ in comparison with $\text{Ni}_2\text{P}_4\text{O}_{12}/\text{RGO}$ and $\text{FeP}_x\text{O}_y/\text{RGO}$, Tafel plots were calculated from LSV curves to assess their reaction kinetic (Fig. 2b). The Tafel slope for $\text{Fe}_x\text{Ni}_{2-x}\text{P}_4\text{O}_{12}/\text{RGO}$ is 43.8 mV dec^{-1} , which is distinctly smaller than those of $\text{Ni}_2\text{P}_4\text{O}_{12}/\text{RGO}$ ($103.3 \text{ mV dec}^{-1}$) and $\text{FeP}_x\text{O}_y/\text{RGO}$

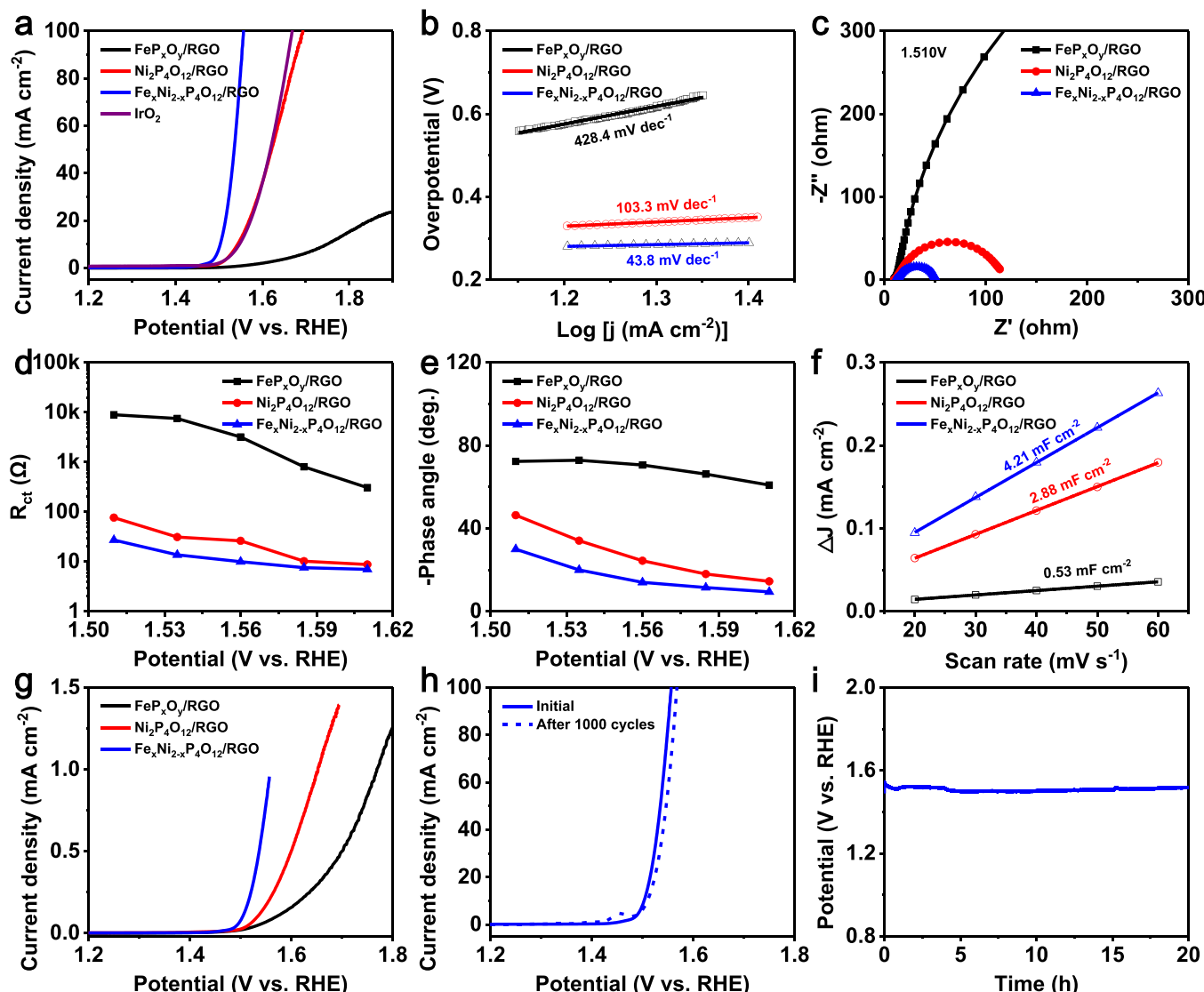


Fig. 3. (a) LSV curves of $\text{Ni}_2\text{P}_4\text{O}_{12}/\text{RGO}$, $\text{FeP}_x\text{O}_y/\text{RGO}$, $\text{Fe}_x\text{Ni}_{2-x}\text{P}_4\text{O}_{12}/\text{RGO}$ and IrO_2 , (b) Tafel slope, (c) EIS plots measured at 1.510 V vs. RHE, (d) R_{ct} values at different potentials, (e) phase angles values at different potentials, (f) C_{dl} and (g) specific activity of $\text{Ni}_2\text{P}_4\text{O}_{12}/\text{RGO}$, $\text{FeP}_x\text{O}_y/\text{RGO}$ and $\text{Fe}_x\text{Ni}_{2-x}\text{P}_4\text{O}_{12}/\text{RGO}$, (h) LSV curves of $\text{Fe}_x\text{Ni}_{2-x}\text{P}_4\text{O}_{12}/\text{RGO}$ initially and after 1000 cycles CV scanning and (i) durability test for $\text{Fe}_x\text{Ni}_{2-x}\text{P}_4\text{O}_{12}/\text{RGO}$ by chronopotentiometry test.

RGO (428.4 mV dec⁻¹). This smallest Tafel slope reveals the fastest reaction kinetic on Fe_xNi_{2-x}P₄O₁₂/RGO surface [36]. EIS technique was further conducted to probe the charge transfer properties. The EIS at 1.510 V vs. RHE were firstly collected. Compared with Ni₂P₄O₁₂/RGO and FeP_xO_y/RGO, the Nyquist plots of Fe_xNi_{2-x}P₄O₁₂/RGO exhibits the smallest semicircle radius (Fig. 3c), indicating its smallest charge transfer resistance (R_{ct}) [37]. Then the EIS measured at different potentials were collected (Fig. S21) and further fitted based on the equivalent circuit model in Fig. S22. Apparently, Fe_xNi_{2-x}P₄O₁₂/RGO always possesses the smallest R_{ct} values among the fabricated samples with increasing potential (Fig. 3d), further confirming its fastest charge transfer kinetics [38]. Besides, the Bode phase plots of all samples exhibit a transition peak corresponding to OER process [39], and the phase angle of transition peak for Fe_xNi_{2-x}P₄O₁₂/RGO gradually decreases and moves to higher frequency region with increasing potential, suggesting its accelerated OER process (Fig. S23). The smallest phase angle of transition peak for Fe_xNi_{2-x}P₄O₁₂/RGO affirms its fastest charge transfer kinetics (Fig. 3e) [40–42].

The activity of electrocatalyst is closely associated with the quantity of exposed active sites, which can be estimated by electrochemical surface area (ECSA). Since the ECSA is linearly proportional to C_{dl} , the C_{dl} was first evaluated by CV measurements at different scan rates [43, 44]. By fitting the capacitance current in CV curves (Fig. S24), the calculated C_{dl} for Fe_xNi_{2-x}P₄O₁₂/RGO (4.21 mF cm⁻²) is considerably higher than that of Ni₂P₄O₁₂/RGO (2.88 mF cm⁻²) and FeP_xO_y/RGO (0.53 mF cm⁻²) (Fig. 3f). After normalizing C_{dl} by a reference specific capacitance (40 μF cm⁻²) [45], the calculated ECSA for Fe_xNi_{2-x}P₄O₁₂, Ni₂P₄O₁₂/RGO and FeP_xO_y/RGO is 105.25, 72 and 13.25 cm⁻², respectively, being indicative that introducing of Fe enable considerable enrichment of activity sites and make an important contribution to the enhanced OER activity. Moreover, LSV current was normalized by ECSA to exclude the influence of the ECSA on OER activity and evaluate the intrinsic activity of each site. As displayed in Fig. 3g, Fe_xNi_{2-x}P₄O₁₂/RGO also possesses the largest specific current density among the three fabricated samples, revealing its highest intrinsic activity [46]. Considering their slight difference in specific surface areas (Fig. S25), the improved OER activity of Fe_xNi_{2-x}P₄O₁₂/RGO should be attributed to its increased quantity and improved intrinsic activity of active site contributed by introducing of Fe. The incorporating of Fe can adjust the electronic structure of the active sites to optimize the adsorption capacity for intermediates, as well as crease some local defects to provide extra active sites, thus leading to increased quantity and improved intrinsic activity of active site [26, 47].

Aside from excellent OER activity, durability is also a key criterion for electrocatalyst. Continuous CV scanning was first performed to assess the durability of Fe_xNi_{2-x}P₄O₁₂/RGO. After successive 1000 cycles CV scanning, the LSV curves only slightly shifts toward higher potential (Fig. 3h), indicating its highly long-term durability. Moreover, long-term chronopotentiometry test curves also display no significant variation in potential (Fig. 3i), further confirming its excellent long-term durability. After durability test, TEM was adopted to investigate the structural evolution of Fe_xNi_{2-x}P₄O₁₂/RGO during durability test. No obvious difference on contrast can be observed in nanoparticle from TEM images (Fig. S26). After durability test, the diffraction peaks assigned to Ni₂P₄O₁₂ disappear (Fig. S27a) and a broad band centered at about 557 cm⁻¹ corresponded to metal (oxy)hydroxide are observed in the Raman spectra (Fig. S27b) [48, 49], indicating the structural reconstruction during OER process. For the XPS spectra of Fe_xNi_{2-x}P₄O₁₂/RGO after durability test, the intensity of Ni 2p and Fe 2p peak was obvious enhanced (Fig. S28a and S28b). This can be attributed to the increased expose of metal center resulted from the structural reconstruction and the removal of carbon on nanoparticles surface [50]. However, the intensity of P 2p peak was significantly reduced and the concentration of P in electrolyte was distinctly increased after durability test, indicating the leaching of P element during durability test process (Fig. S28c and S29a). The leaching of P element can create some

vacancies to provide extra active and optimize the adsorption capacity for intermediates [51, 52], which are conducive to OER process. In addition, the leached phosphate group can re-adsorb on the surface of electrocatalyst during OER process, which can also regulate the electronic structure of the electrocatalyst and ensure durability [53, 54]. As for Ni and Fe elements, no obvious leaching was observed (Fig. S29b–c). These results confirm that structural reconstruction occurs during OER process, resulted in the formation of metal (oxy)hydroxides. According to literatures, this formed metal (oxy)hydroxides can offer the real active centers for OER [55].

3.3. Mechanism analysis of enhanced OER activity

The introducing of Fe can cause the charge redistribution of Fe_xNi_{2-x}P₄O₁₂/RGO, and thus adjust the electronic structure to optimize the adsorption capability for OER intermediates. To further explore the reason of improved OER activity of Fe_xNi_{2-x}P₄O₁₂/RGO, we investigated the adsorption capability of as-fabricated samples toward OER intermediates. Previous researches have demonstrated that *OH is a very important intermediate during OER process and its binding capability is corrected with binding capability of other oxygen-containing intermediates [56]. The intermediate of *OH is electrophiles, which can be captured by the reagent with nucleophiles, such as methanol [56, 57]. Therefore, LSV current of as-fabricated samples were further collected in the presence of methanol to estimate the influence of incorporated Fe on the adsorption capability of *OH. As depicted in Fig. 4a, much greater increased current density was observed in the LSV curves of Ni₂P₄O₁₂/RGO, revealing higher *OH coverage on the surface of Ni₂P₄O₁₂/RGO. While for FeP_xO_y/RGO, much lower methanol oxidation current are observed in comparison with Ni₂P₄O₁₂/RGO (Fig. 4b), indicating its lower *OH surface coverage [57]. For Fe_xNi_{2-x}P₄O₁₂/RGO, only slightly current difference was observed on the LSV curves (Fig. 4c). This reflects its optimized adsorption capability toward *OH. These results indicate that incorporating of Fe can adjust the adsorption characteristic of *OH to optimized value, thus causing to the enhanced OER activity. The valence electron configuration of Ni²⁺ is t₂⁶g₆² and its t_{2g} is fully occupied (Fig. 4d), therefore, the interaction force between Ni²⁺ and its bridging O²⁻ is electron-electron repulsion interaction (Fig. 4e) [58]. For Fe³⁺, its valence electronic configuration is t₂³g₆² and its t_{2g} contains three unpaired electrons. Hence, the π-donation is the mainly interaction force between Fe³⁺ and its bridging O²⁻ [59]. After coupling between Ni²⁺ and Fe³⁺, the electron-electron repulsion between Ni²⁺ and O²⁻ would trigger partial electron transfers from Ni to Fe, resulting in the redistribution of electron [60]. This agrees well with the results of XPS analysis. As a consequence, the adsorption capability of *OH was optimized.

To deeply understand the effects of the incorporated Fe on the improved OER activity of Fe_xNi_{2-x}P₄O₁₂/RGO, density functional theory (DFT) calculations were conducted. According to HRTEM results, (−113) surface was chose to construct theoretical models (Fig. 5a). The ratio of Fe:Ni is based on that in crystalline region. The differential density of state (DOS) of Ni d-orbitals in Fe_xNi_{2-x}P₄O₁₂ and Ni₂P₄O₁₂ (Fig. 5b) reveals that incorporating Fe can observably induce the electron arrangement because of different electronegativity of Fe and Ni. Moreover, the calculated d-band center of the Ni was upshift from −2.495 eV to −2.475 eV after incorporating Fe, illustrating the increased bonding strength between active sites and intermediates [61]. Afterwards, the OER reaction pathway of Fe_xNi_{2-x}P₄O₁₂ and Ni₂P₄O₁₂ was further investigated. The reaction step with maximal changes of Gibbs free energies (ΔG) is the rate-determining step (RDS). For Ni₂P₄O₁₂, the RDS is the formation *O from *OH with the maximal ΔG value of 2.06 eV (Fig. 5c), thus resulting in the higher *OH coverage on the surface of Ni₂P₄O₁₂. After incorporating Fe, the energy barrier for RDS decreases to 1.98 eV, revealing more favorable OER thermodynamics. The above DFT calculation results confirm that incorporating Fe can cause the redistribution of electron to optimize the adsorption

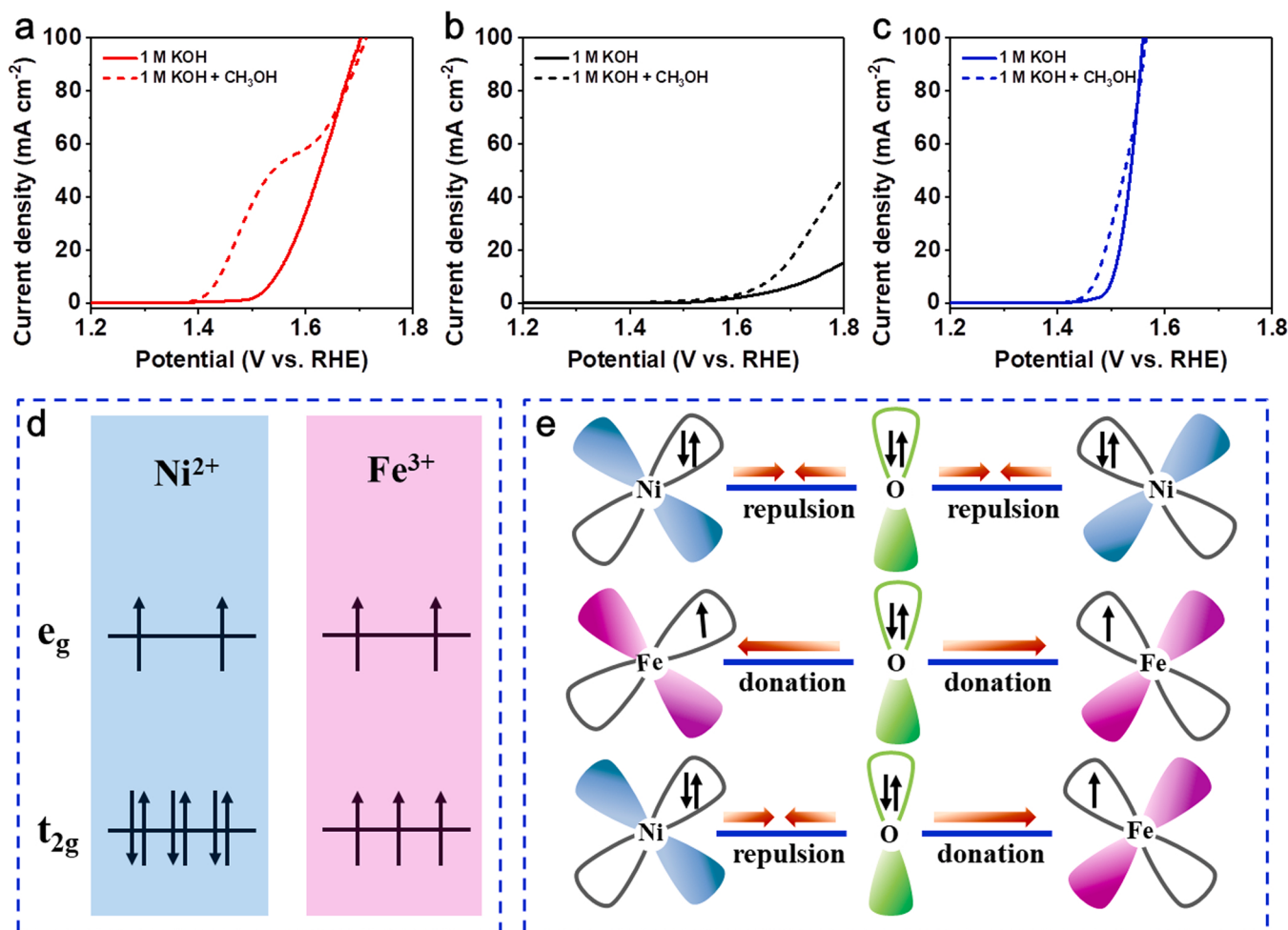


Fig. 4. The LSV curves of (a) Ni₂P₄O₁₂/RGO, (b) FeP_xO_y/RGO and (c) Fe_xNi_{2-x}P₄O₁₂/RGO in 1 M KOH with and without methanol, (d) schematic illustration of electron configurations of 3d orbitals and (e) the electron coupling between Ni²⁺ and Fe³⁺.

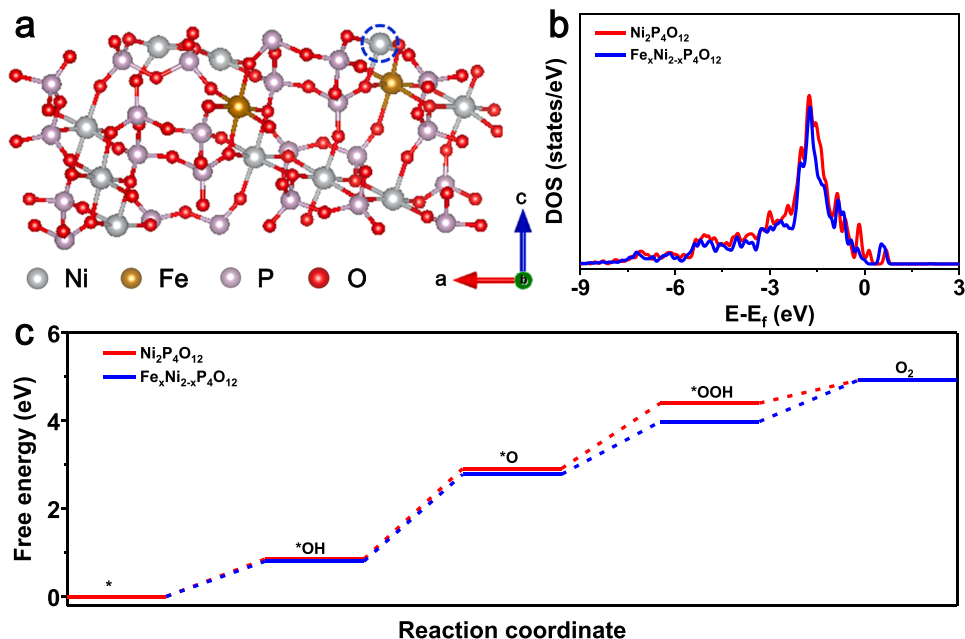


Fig. 5. (a) Atomic structure model of Fe_xNi_{2-x}P₄O₁₂ for DFT calculation, the active sites was marked by blue circle, (b) DOS of Fe_xNi_{2-x}P₄O₁₂ and Ni₂P₄O₁₂, (c) OER free energy diagrams of Fe_xNi_{2-x}P₄O₁₂ and Ni₂P₄O₁₂.

capability for intermediates, thus ensuring a high OER activity. Besides, considering different Fe content in crystalline and amorphous region, the OER reaction pathway of $\text{Fe}_x\text{Ni}_{2-x}\text{P}_4\text{O}_{12}$ with a higher Fe content based on that in amorphous region was also investigated. Because amorphous materials are very difficult to construct model, model with crystalline structure was employed (Fig. S30a). After incorporating Fe with higher level, the RDS changes to generate $^{\bullet}\text{O}$ from $^{\bullet}\text{OH}$ with the energy barrier of 1.79 eV (Fig. S30b), demonstrating its further improved OER activity in comparison with $\text{Ni}_2\text{P}_4\text{O}_{12}$. Furthermore, considering higher ratio of Fe:Ni, the possibility of Fe being active sites was also investigated. The calculated results reveal that the Ni atoms are the active sites because of their smaller energy barrier for RDS in comparison with that on Fe sites (2.16 eV).

3.4. Electrocatalytic water splitting performance

Considering application, commercial NFF with excellent conductivity and highly porosity (Fig. S31) was utilized as substrate to load $\text{Fe}_x\text{Ni}_{2-x}\text{P}_4\text{O}_{12}/\text{RGO}$. As presented in Fig. 6a, the activity of $\text{Fe}_x\text{Ni}_{2-x}\text{P}_4\text{O}_{12}/\text{RGO}$ loaded on NFF is also superior to that of IrO_2 . Specifically, $\text{Fe}_x\text{Ni}_{2-x}\text{P}_4\text{O}_{12}/\text{RGO}$ only requires overpotential of 258, 277, 340 and 380 mV to achieve 50, 100, 500 and 1000 mA cm⁻², respectively, which is obviously smaller than those of IrO_2 (291, 314, 425 and 522 mV) and many recently reported phosphate based OER electrocatalyst (Table S2). To further evaluate the feasibility of $\text{Fe}_x\text{Ni}_{2-x}\text{P}_4\text{O}_{12}/\text{RGO}$ as a high-efficiency anode electrocatalyst for water splitting, an overall water splitting device consisting of $\text{Fe}_x\text{Ni}_{2-x}\text{P}_4\text{O}_{12}/\text{RGO}$ as anode and Pt/C as cathode was also assembled. The corresponding LSV curves reveal that Pt/C|| $\text{Fe}_x\text{Ni}_{2-x}\text{P}_4\text{O}_{12}/\text{RGO}$ cell possesses excellent overall water splitting activity (Fig. 6b), requiring cell voltage of 1.519, 1.549, 1.678 and 1.773 to reach 50, 100, 500 and 1000 mA cm⁻², respectively, which are much superior to the Pt/C|| IrO_2 pairs. Besides outstanding activity, long-term durability is an essential part of assessing electrode for

electrolytic water splitting. As evident from Fig. 6c, the voltage can hold relatively steady during 100 h continuous electrolysis at 100 mA cm⁻², confirming the excellent durability of the Pt/C|| $\text{Fe}_x\text{Ni}_{2-x}\text{P}_4\text{O}_{12}/\text{RGO}$ cell. In addition, the Faradaic efficiency of the Pt/C|| $\text{Fe}_x\text{Ni}_{2-x}\text{P}_4\text{O}_{12}/\text{RGO}$ cell was also evaluated to explore the conversion efficiency of electrons. The measured volumes of H_2 and O_2 have a high coincidence with the theoretical value, and the ratio of their volume is approximately 2:1 (Fig. S32), confirming their close to 100% Faradaic efficiency. All aforementioned results successfully demonstrate the potential of $\text{Fe}_x\text{Ni}_{2-x}\text{P}_4\text{O}_{12}/\text{RGO}$ as a highly efficient anodic catalyst for water splitting.

4. Conclusions

In summary, we develop a novel and facile approach to fabricate $\text{Fe}_x\text{Ni}_{2-x}\text{P}_4\text{O}_{12}/\text{RGO}$ hybrids as highly performance OER electrocatalyst. The heating treatment process for presented strategy can not only be achieved within a short period, but also avoid generating toxic PH_3 gas, which are greatly favorable for large-scale application. Thanks to abundant accessible active sites, optimized adsorption capability for OER intermediates and enhanced conductivity, the resulted $\text{Fe}_x\text{Ni}_{2-x}\text{P}_4\text{O}_{12}/\text{RGO}$ hybrid exhibit remarkable OER activity, with small overpotential of 258, 277, 340 and 380 mV at 50, 100, 500 and 1000 mA cm⁻². Moreover, the electrolytic cell assembled by Pt/C and $\text{Fe}_x\text{Ni}_{2-x}\text{P}_4\text{O}_{12}/\text{RGO}$ also displays excellent activity toward water splitting, which merely needs cell voltage of 1.519, 1.549, 1.678 and 1.773 to achieve 50, 100, 500 and 1000 mA cm⁻², respectively, as well as outstanding durability at 100 mA cm⁻² for 100 h, demonstrating its potential as high-performance OER electrocatalyst. This work affords a high-efficiency OER electrocatalyst, along with a novel approach to synthesize other transition metal phosphate based electrocatalyst.

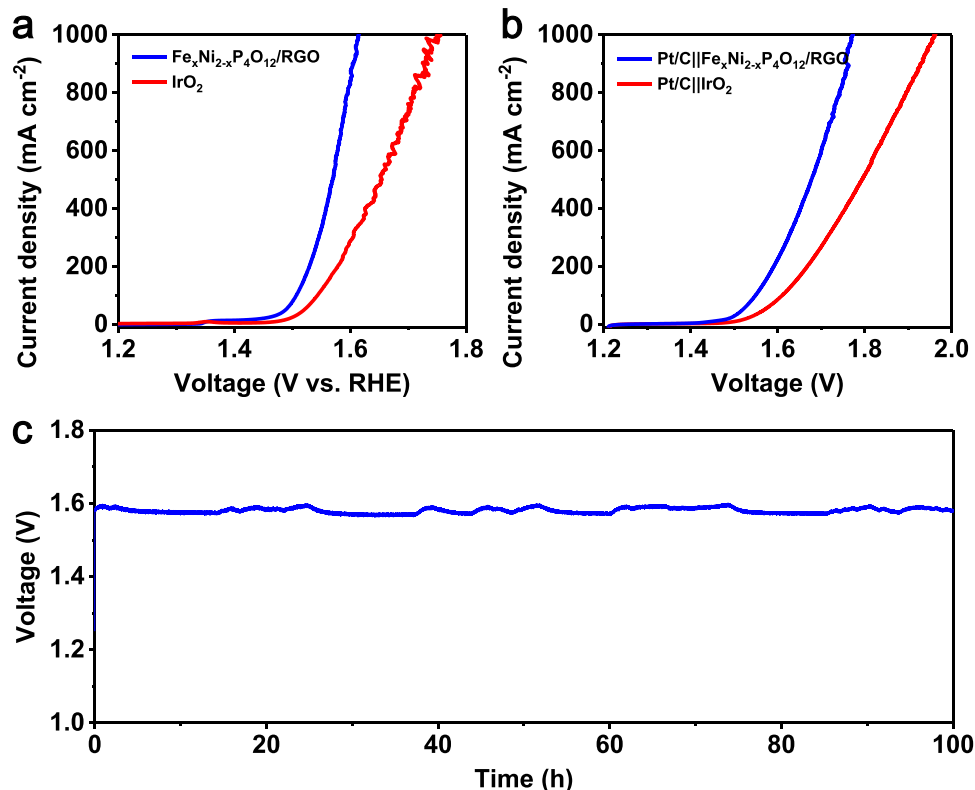


Fig. 6. (a) The comparison of LSV curves of $\text{Fe}_x\text{Ni}_{2-x}\text{P}_4\text{O}_{12}/\text{RGO}$ and IrO_2 loaded on NFF, (b) LSV curves of Pt/C|| $\text{Fe}_x\text{Ni}_{2-x}\text{P}_4\text{O}_{12}/\text{RGO}$ and Pt/C|| IrO_2 pairs and (c) durability test for electrolytic cell assembled by Pt/C|| $\text{Fe}_x\text{Ni}_{2-x}\text{P}_4\text{O}_{12}/\text{RGO}$ through chronopotentiometry test at 100 mA cm⁻².

CRediT authorship contribution statement

Lu Lin: Conceptualization, Investigation, Data curation, Writing – original draft. **Yufeng Wang:** Investigation, Data curation, Formal analysis, Writing – original draft. **Qing Ye:** Investigation, Data curation, Formal analysis, Writing – original draft. **Yanxia Zhao:** Resources, Funding acquisition, Supervision, Visualization, Writing – review & editing. **Yongliang Cheng:** Conceptualization, Funding acquisition, Project administration, Supervision, Writing – review & editing.

Declaration of Competing Interest

The authors declare that they have no known competing financial interests or personal relationships that could have appeared to influence the work reported in this paper.

Data Availability

Data will be made available on request.

Acknowledgements

This work was financially supported by National Natural Science Foundation of China (21875187, 61971211, 22171222) and the Key projects of intergovernmental international cooperation in key R & D programs of the Ministry of Science and Technology of China (2021YFE0115800).

Appendix A. Supporting information

Supplementary data associated with this article can be found in the online version at [doi:10.1016/j.apcatb.2023.122834](https://doi.org/10.1016/j.apcatb.2023.122834).

References

- [1] M. Chatenet, B.G. Pollet, D.R. Dekel, F. Dionigi, J. Deseure, P. Millet, R.D. Braatz, M.Z. Bazant, M. Eikerling, I. Staffell, P. Balcombe, Y. Shao-Horn, H. Schäfer, Water electrolysis: from textbook knowledge to the latest scientific strategies and industrial developments, *Chem. Soc. Rev.* 51 (2022) 4583–4762.
- [2] H. Ding, H. Liu, W. Chu, C. Wu, Y. Xie, Structural transformation of heterogeneous materials for electrocatalytic oxygen evolution reaction, *Chem. Rev.* 121 (2021) 13174–13212.
- [3] Q. Liu, M. Ranocchiai, J.A. van Bokhoven, Catalyst overcoating engineering towards high-performance electrocatalysis, *Chem. Soc. Rev.* 51 (2022) 188–236.
- [4] Z.-Y. Yu, Y. Duan, X.-Y. Feng, X. Yu, M.-R. Gao, S.-H. Yu, Clean and affordable hydrogen fuel from alkaline water splitting: past, recent progress, and future prospects, *Adv. Mater.* 33 (2021), 2007100.
- [5] T.Q. Guo, L.D. Li, Z.C. Wang, Recent development and future perspectives of amorphous transition metal-based electrocatalysts for oxygen evolution reaction, *Adv. Energy Mater.* 12 (2022), 2200827.
- [6] Z. Wei, M. Guo, Q. Zhang, Scalable electrodeposition of NiFe-based electrocatalysts with self-evolving multi-vacancies for high-performance industrial water electrolysis, *Appl. Catal. B-Environ.* 322 (2023), 122101.
- [7] Y. Shao, X. Xiao, Y.P. Zhu, T.Y. Ma, Single-crystal cobalt phosphate nanosheets for biomimetic oxygen evolution in neutral electrolytes, *Angew. Chem. Int. Ed.* 58 (2019) 14599–14604.
- [8] H. Cao, P. Qiao, Q. Zhong, R. Qi, Y. Dang, L. Wang, Z. Xu, W. Zhang, In situ reconstruction Ni-O octahedral active sites for promoting electrocatalytic oxygen evolution of nickel phosphate, *Small* 19 (2023), e2204864.
- [9] J. Huang, Y. Sun, Y. Zhang, G. Zou, C. Yan, S. Cong, T. Lei, X. Dai, J. Guo, R. Lu, Y. Li, J. Xiong, A new member of electrocatalysts based on nickel metaphosphate nanocrystals for efficient water oxidation, *Adv. Mater.* 30 (2018) 1705045 (n/a).
- [10] Y. Li, Z. Wang, J. Hu, S. Li, Y. Du, X. Han, P. Xu, Metal-organic frameworks derived interconnected bimetallic metaphosphate nanoarrays for efficient electrocatalytic oxygen evolution, *Adv. Funct. Mater.* 30 (2020), 1910498.
- [11] Y. Hu, Y. Zhang, C. Li, L. Wang, Y. Du, G. Mo, X. Li, A.K. Cheetham, J. Wang, Guided assembly of microporous/mesoporous manganese phosphates by bifunctional organophosphonic acid etching and templating, *Adv. Mater.* 31 (2019), e1901124.
- [12] S. Sultan, M. Ha, D.Y. Kim, J.N. Tiwari, C.W. Myung, A. Meena, T.J. Shin, K. H. Chae, K.S. Kim, Superb water splitting activity of the electrocatalyst $\text{Fe}_3\text{Co}(\text{PO}_4)_4$ designed with computation aid, *Nat. Commun.* 10 (2019) 5195.
- [13] D. Liang, C. Lian, Q. Xu, M. Liu, H. Liu, H. Jiang, C. Li, Interfacial charge polarization in $\text{Co}_2\text{P}_2\text{O}_7/\text{N}$, P co-doped carbon nanocages as Mott-Schottky electrocatalysts for accelerating oxygen evolution reaction, *Appl. Catal. B-Environ.* 268 (2020), 118417.
- [14] R. Gond, D.K. Singh, M. Eswaramoorthy, P. Barpanda, Sodium cobalt metaphosphate as an efficient oxygen evolution reaction catalyst in alkaline solution, *Angew. Chem. Int. Ed.* 58 (2019) 8330–8335.
- [15] C. Murugesan, S.P. Panjalingam, S. Lochab, R.K. Rai, X. Zhao, D. Singh, R. Ahuja, P. Barpanda, Cobalt tetraphosphate as an efficient bifunctional electrocatalyst for hybrid sodium-air batteries, *Nano Energy* 89 (2021), 106485.
- [16] J. Wang, J. Hu, S. Niu, S. Li, Y. Du, P. Xu, Crystalline-amorphous $\text{Ni}_2\text{P}_4\text{O}_{12}/\text{NiMoO}_x$ nanoarrays for alkaline water electrolysis: enhanced catalytic activity via in situ surface reconstruction, *Small* 18 (2022), e2105972.
- [17] J. Luo, Y. Liu, H. Xiao, Y. Wang, Y. Mao, Y. Zhang, Y. Su, Y. Xia, S. Chen, Q. Deng, Z. Zeng, S. Deng, J. Wang, Nickel-cobalt cyclo-tetraphosphate decorated hollow carbon nanocages as effective polysulfide promoters for stable lithium-sulfur batteries, *Chem. Eng. J.* 451 (2023), 138677.
- [18] D. Chinnadurai, R. Rajendran, O.L. Li, K. Prabakar, Mn-Co bimetallic phosphate on electrodeposited PANI nanowires with composition modulated structural morphology for efficient electrocatalytic water splitting, *Appl. Catal. B-Environ.* 292 (2021), 120202.
- [19] Y. Wu, Y. Deng, J. Zhang, S. Lv, Z. Xiao, L. Liu, X. Jia, C. Chen, Z. Dang, Z. Li, L. Wang, Construction of multi-channel basic cobalt/nickel phosphate core-shell microsphere for superior hybrid Zn-based supercapacitor performances, *Chem. Eng. J.* 455 (2023), 140953.
- [20] Z. Wang, X. Zhang, X. Wu, Y. Pan, H. Li, Y. Han, G. Xu, J. Chi, J. Lai, L. Wang, High-entropy phosphate/C hybrid nanosheets for efficient acidic hydrogen evolution reaction, *Chem. Eng. J.* 437 (2022), 135375.
- [21] K. Li, J. Ma, X. Guan, H. He, M. Wang, G. Zhang, F. Zhang, X. Fan, W. Peng, Y. Li, 3D self-supported $\text{Ni}(\text{PO}_3)_2\text{-Moo}_3$ nanorods anchored on nickel foam for highly efficient overall water splitting, *Nanoscale* 10 (2018) 22173–22179.
- [22] L. Peng, M. Liao, X. Zheng, Y. Nie, L. Zhang, M. Wang, R. Xiang, J. Wang, L. Li, Z. Wei, Accelerated alkaline hydrogen evolution on $\text{M(OH)}_x/\text{M-MoPO}_x$ ($\text{M} = \text{Ni}, \text{Co}, \text{Fe}, \text{Mn}$) electrocatalysts by coupling water dissociation and hydrogen adsorption steps, *Chem. I. Sci.* 11 (2020) 2487–2493.
- [23] Z. Zhou, L. Zeng, G. Xiong, L. Yang, H. Yuan, J. Yu, S. Xu, D. Wang, X. Zhang, H. Liu, W. Zhou, Multifunctional electrocatalyst of NiCo-NiCoP nanoparticles embedded into P-doped carbon nanotubes for energy-saving hydrogen production and upgraded conversion of formaldehyde, *Chem. Eng. J.* 426 (2021), 129214.
- [24] Y. Zhang, T. Gao, Z. Jin, X. Chen, D. Xiao, A robust water oxidation electrocatalyst from amorphous cobalt–iron bimetallic phytate nanostructures, *J. Mater. Chem. A* 4 (2016) 15888–15895.
- [25] R. Hu, H.Y. Jiang, J.L. Xian, S.Y. Mi, L.Y. Wei, G.Y. Fang, J.Y. Guo, S.Q. Xu, Z. Y. Liu, H.Y. Jin, W.L. Xu, J. Wan, Microwave-pulse sugar-blowing assisted synthesis of 2D transition metal carbides for sustainable hydrogen evolution, *Appl. Catal. B-Environ.* 317 (2022), 121728.
- [26] X. Yu, Q. Lv, L. She, L. Hou, Y. Fautrelle, Z. Ren, G. Cao, X. Lu, X. Li, Controlled moderate sulfidation-fabricated hierarchical heterogeneous nickel sulfides-based electrocatalyst with tripartite Mo doping for efficient oxygen evolution, *J. Energy Chem.* 68 (2022) 780–788.
- [27] D.J. Zhou, Y. Jia, X.X. Duan, J.L. Tang, J. Xu, D. Liu, X.Y. Xiong, J.M. Zhang, J. Luo, L.R. Zheng, B. Liu, Y. Kuang, X.M. Sun, X. Duan, Breaking the symmetry: Gradient in NiFe layered double hydroxide nanoarrays for efficient oxygen evolution, *Nano Energy* 60 (2019) 661–666.
- [28] D. Cheng, Z. Wang, C. Chen, K. Zhou, Crystalline/amorphous $\text{Co}_2\text{P}/\text{FePO}_4$ core/shell nanoheterostructures supported on porous carbon microspheres as efficient oxygen reduction electrocatalysts, *Chem. Mater.* 31 (2019) 8026–8034.
- [29] Y. Zheng, X. Wang, W. Zhao, X. Cao, J. Liu, Phytic acid-assisted synthesis of ultrafine NiCo_2S_4 nanoparticles immobilized on reduced graphene oxide as high-performance electrode for hybrid supercapacitors, *Chem. Eng. J.* 333 (2018) 603–612.
- [30] Y. Liu, S. He, B. Huang, Z. Kong, L. Guan, Influence of different Fe doping strategies on modulating active sites and oxygen reduction reaction performance of Fe, N-doped carbonaceous catalysts, *J. Energy Chem.* 70 (2022) 511–520.
- [31] C. Zhu, F. Liu, C. Ling, H. Jiang, H. Wu, A. Li, Growth of graphene-supported hollow cobalt sulfide nanocrystals via MOF-templated ligand exchange as surface-bound radical sinks for highly efficient bisphenol A degradation, *Appl. Catal. B-Environ.* 242 (2019) 238–248.
- [32] Y. Zhang, L. Chen, B. Yan, F. Zhang, Y. Shi, X. Guo, Regeneration of textile sludge into Cu8S5 decorated N, S self-doped interconnected porous carbon as an advanced bifunctional electrocatalyst for overall water splitting, *Chem. Eng. J.* 451 (2023), 138497.
- [33] L.X. Zhou, Q.H. Liu, X.L. Ma, P.P. Sun, X.W. Lv, L. Fang, X.H. Sun, M.H. Shang, High areal energy density and super durable aqueous rechargeable NiCo//Zn battery with hierarchical structural cobalt-nickel phosphate octahydrate as binder-free cathode, *Chem. Eng. J.* 450 (2022), 138035.
- [34] L. Li, G.W. Zhang, B. Wang, S.C. Yang, Constructing the Fe/Cr double (oxy) hydroxides on Fe_3O_4 for boosting the electrochemical oxygen evolution in alkaline seawater and domestic sewage, *Appl. Catal. B-Environ.* 302 (2022), 120847.
- [35] X. Liu, B. Wen, R. Guo, J. Meng, Z. Liu, W. Yang, C. Niu, Q. Li, L. Mai, A porous nickel cyclotetraphosphate nanosheet as a new acid-stable electrocatalyst for efficient hydrogen evolution, *Nanoscale* 10 (2018) 9856–9861.
- [36] F. Yang, J. Xie, D. Rao, X. Liu, J. Jiang, X. Lu, Octahedral distortion enhances exceptional oxygen catalytic activity of calcium manganite for advanced Zn-air batteries, *Nano Energy* 85 (2021), 106020.
- [37] Q. Ye, J. Liu, L. Lin, M. Sun, Y. Wang, Y. Cheng, Fe and P dual-doped nickel carbonate hydroxide/carbon nanotube hybrid electrocatalysts for an efficient oxygen evolution reaction, *Nanoscale* 14 (2022) 6648–6655.

- [38] J. Hu, D. Jiang, Z. Weng, Y. Pan, Z. Li, H. Du, Y. Yuan, A universal electrochemical activation enabling lattice oxygen activation in nickel-based catalyst for efficient water oxidation, *Chem. Eng. J.* 430 (2022), 132736.
- [39] H. He, L. Zeng, X. Peng, Z. Liu, D. Wang, B. Yang, Z. Li, L. Lei, S. Wang, Y. Hou, Porous cobalt sulfide nanosheets arrays with low valence copper incorporated for boosting alkaline hydrogen evolution via lattice engineering, *Chem. Eng. J.* 451 (2023), 138628.
- [40] C. Yang, L. Zhou, C. Wang, W. Duan, L. Zhang, F. Zhang, J. Zhang, Y. Zhen, L. Gao, F. Fu, Y. Liang, Large-scale synthetic Mo@(²H-¹T)-MoSe₂ monolithic electrode for efficient hydrogen evolution in all pH scale ranges and seawater, *Appl. Catal. B-Environ.* 304 (2022), 120993.
- [41] T.W. Zhao, X.J. Shen, Y. Wang, R.K. Hocking, Y.B. Li, C.L. Rong, K. Dastafkan, Z. Su, C. Zhao, In situ reconstruction of V-doped Ni₂P pre-catalysts with tunable electronic structures for water oxidation, *Adv. Funct. Mater.* 31 (2021), 2100614.
- [42] Y. Wang, Y. Zheng, J. Xie, M. Lv, J. Luo, F. Yang, Y. Yu, X. Lu, Iron-induced electron modulation of nickel hydroxide/carbon nanotubes composite to effectively boost the oxygen evolution activity, *Chem. Eng. J.* 452 (2023), 139369.
- [43] Q. Wang, H. Xu, X. Qian, G. He, H. Chen, Sulfur vacancies engineered self-supported Co₃S₄ nanoflowers as an efficient bifunctional catalyst for electrochemical water splitting, *Appl. Catal. B-Environ.* 322 (2023), 122104.
- [44] F. Yang, X. Zhang, L. Zhou, S. Lin, X. Cao, J. Jiang, X. Lu, Tuning the interfacial electronic coupling of NiO via CeO₂ and nitrogen co-decoration for highly efficient oxygen evolution reaction, *Chem. Eng. J.* 432 (2022), 134255.
- [45] P. Sun, Y. Zhou, H. Li, H. Zhang, L. Feng, Q. Cao, S. Liu, T. Wågberg, G. Hu, Round-the-clock bifunctional honeycomb-like nitrogen-doped carbon-decorated Co₂P/Mo₂C-heterojunction electrocatalyst for direct water splitting with 18.1% STH efficiency, *Appl. Catal. B-Environ.* 310 (2022), 121354.
- [46] Y.Y. Song, J.L. Cheng, J. Liu, Q. Ye, X. Gao, J.J. Lu, Y.L. Cheng, Modulating electronic structure of cobalt phosphide porous nanofiber by ruthenium and nickel dual doping for highly-efficiency overall water splitting at high current density, *Appl. Catal. B-Environ.* 298 (2021), 120488.
- [47] S. Wang, X. Liu, X. Chen, K. Dastafkan, Z.-H. Fu, X. Tan, Q. Zhang, C. Zhao, Superexchange effect induced by early 3d metal doping on NiFe₂O₄ (001) surface for oxygen evolution reaction, *J. Energy Chem.* 78 (2023) 21–29.
- [48] X. Liu, J. Huang, T.T. Li, W. Chen, G.L. Chen, L.T. Han, K. Ostrikov, High-efficiency oxygen evolution catalyzed by Sn-Co-Ni phosphide with oriented crystal phases, *J. Mater. Chem. A* 10 (2022) 13448–13455.
- [49] R.P. Luo, Y.Y. Li, L.X. Xing, R.Y. Zhong, Z.Y. Qian, G.P. Yin, Y.C. Wang, L. Du, A dynamic Ni(OH)₂-NiOOH/NiFeP heterojunction enabling high-performance E-upgrading of hydroxymethylfurfural, *Appl. Catal. B-Environ.* 311 (2022), 121357.
- [50] H.J. Song, H. Yoon, B. Ju, D.-Y. Lee, D.-W. Kim, Electrocatalytic selective oxygen evolution of carbon-coated Na₂Co_{1-x}Fe_xP₂O₇ nanoparticles for alkaline seawater electrolysis, *ACS Catal.* 10 (2020) 702–709.
- [51] Y.H. Tian, X.Z. Liu, L. Xu, D. Yuan, Y.H. Dou, J.X. Qiu, H.N. Li, J.M. Ma, Y. Wang, D. Su, S.Q. Zhang, Engineering crystallinity and oxygen vacancies of Co(II) oxide nanosheets for high performance and robust rechargeable Zn-air batteries, *Adv. Funct. Mater.* 31 (2021), 2101239.
- [52] X.-Y. Zhang, F.-T. Li, Y.-W. Dong, B. Dong, F.-N. Dai, C.-G. Liu, Y.-M. Chai, Dynamic anion regulation to construct S-doped FeOOH realizing 1000 mA cm⁻²-level-current-density oxygen evolution over 1000h, *Appl. Catal. B-Environ.* 315 (2022), 121571.
- [53] X. Chen, Z. Qiu, H. Xing, S. Fei, J. Li, L. Ma, Y. Li, D. Liu, Sulfur-doping/leaching induced structural transformation toward boosting electrocatalytic water splitting, *Appl. Catal. B-Environ.* 305 (2022), 121030.
- [54] X. Wang, J. Li, Q. Xue, X. Han, C. Xing, Z. Liang, P. Guardia, Y. Zuo, R. Du, L. Balcells, J. Arbiol, J. Llorca, X. Qi, A. Cabot, Sulfate-decorated amorphous-crystalline cobalt-iron oxide nanosheets to enhance O-O coupling in the oxygen evolution reaction, *ACS Nano* 17 (2023) 825–836.
- [55] S. Singh, D.C. Nguyen, N.H. Kim, J.H. Lee, Interface engineering induced electrocatalytic behavior in core-shelled CNTs@NiP₂/NbP heterostructure for highly efficient overall water splitting, *Chem. Eng. J.* 442 (2022), 136120.
- [56] Y.J. Mei, Y.B. Feng, C.X. Zhang, Y. Zhang, Q.L. Qi, J. Hu, High-entropy alloy with Mo-coordination as efficient electrocatalyst for oxygen evolution reaction, *ACS Catal.* 12 (2022) 10808–10817.
- [57] H.B. Tao, Y. Xu, X. Huang, J. Chen, L. Pei, J. Zhang, J.G. Chen, B. Liu, A general method to probe oxygen evolution intermediates at operating conditions, *Joule* 3 (2019) 1498–1509.
- [58] X. Wang, D. Du, H. Xu, Y. Yan, X. Wen, L. Ren, C. Shu, NiMn-based metal-organic framework with optimized eg orbital occupancy as efficient bifunctional electrocatalyst for lithium-oxygen batteries, *Chem. Eng. J.* 452 (2023), 139524.
- [59] C.-F. Li, L.-J. Xie, J.-W. Zhao, L.-F. Gu, H.-B. Tang, L. Zheng, G.-R. Li, Interfacial Fe-O-Ni-O-Fe bonding regulates the active Ni sites of Ni-MOFs via iron doping and decorating with FeOOH for super-efficient oxygen evolution, *Angew. Chem. Int. Ed.* 61 (2022), e202116934.
- [60] Y. Zhai, X. Ren, Y. Sun, D. Li, B. Wang, S. Liu, Synergistic effect of multiple vacancies to induce lattice oxygen redox in NiFe-layered double hydroxide OER catalysts, *Appl. Catal. B-Environ.* 323 (2023), 122091.
- [61] S.F. Zai, X.Y. Gao, C.C. Yang, Q. Jiang, Ce-modified Ni(OH)₂ nanoflowers supported on NiSe₂ octahedra nanoparticles as high-efficient oxygen evolution electrocatalyst, *Adv. Energy Mater.* 11 (2021), 2101266.